SRC TR 89-73

Subband Image Coding Using Entropy-Coded Quantization Over Noisy Channels

By

N. Tanabe and N. Farvardin

Subband Image Coding Using Entropy-Coded Quantization Over Noisy Channels †

N. Tanabe ‡ and N. Farvardin
Electrical Engineering Department
Institute for Advanced Computer Studies
and
Systems Research Center
University of Maryland
College Park, MD 20742

Abstract

In the first part of this paper, under the assumption of noiseless transmission, we develop two entropy-coded subband image coding schemes. The difference between these schemes is the procedure used for encoding the lowest frequency subband: predictive coding is used in one system and transform coding in the other. Other subbands are encoded using zero-memory quantization. After a careful study of subband statistics, the quantization parameters, the corresponding Huffman codes and the bit allocation among subbands are all optimized. It is shown that both schemes perform considerably better than the scheme developed by Woods and O'Neil [2]. Roughly speaking, these new schemes perform the same as that in [2] at half the encoding rate. In the second part of the paper, after demonstrating the unacceptable sensitivity of these schemes to transmission noise, we will develop a combined source/channel coding scheme in which rate-compatible convolutional codes are used to provide protection against channel noise. A packetization scheme to prevent infinite error propagation is used and an algorithm for optimal assignment of bits between the source and channel encoders of different subbands is developed. We will show that, in the presence of channel noise, these channel-optimized schemes offer dramatic performance improvements over the schemes designed based on a noiseless channel assumption; they also perform better than that of [2] even in the absence of channel noise. Finally, the robustness of the proposed schemes against channel mismatch will be studied.

† This work was supported in part by National Science Foundation grants NSFD MIP-86-57311 and NSFD CDR-85-00108, and in part by Mitsubishi Electric Corporation and Martin Marietta Laboratories.

‡ On leave from Mitsubishi Electric Corporation, Tokyo, Japan.

I. Introduction

The concept of subband coding (SBC) was first introduced by Crochiere *et al.* [1] in the context of speech coding. Since then, this technique has received considerable attention as a powerful source coding technique. Recently, Woods and O'Neil [2] extended this concept to the encoding of monochrome images in which a fullband image is split into 16 equally divided subbands, by means of a two-dimensional (2-D) separable quadrature mirror filter (QMF) bank, each of which is encoded by a separate DPCM encoder. A bit allocation procedure is used to distribute the encoding bits among subbands in order to minimize the overall reconstruction mean squared-error (MSE). The development of the subband image coding scheme in [2] is considered an important accomplishment in image coding because it resulted in a coding scheme that performs better than other well-known schemes such as adaptive discrete cosine transform (DCT), vector quantization (VQ) and differential VQ for most bit rates of interest. In addition, it was established in [2] that the SBC has good subjective error properties and is appropriate for progressive image transmissions. These encouraging results have led to a significant amount of research activity on subband image coding.

In another recent paper, Gharavi and Tabatabai [3] have introduced a SBC scheme in which a QMF bank is used to split an image into 7 unequally divided subbands; the lowest frequency subband is encoded by DPCM and the others by zero-memory quantizers. The zero-memory quantizers have a center dead zone to eliminate the picture noise included in the higher frequency subbands. Extensions to color image coding were also considered in [3].

In [4] and [5] the application of VQ to encoding of subbands is considered. Here, VQ is used to encode vectors consisting of samples from different subbands. In [5], for the asymptotic case of high bit rates, the coding gain of VQ over scalar quantization (SQ) is computed analytically. Safranek *et al.* [6] and Kim *et al.* [7] also used VQ in SBC of images, where the VQ is applied within a subband in contrast to [4], [5].

The focus of this paper is twofold: (i) development of more efficient SBC coding schemes for noiseless channels and (ii) study of channel error effects on the performance of SBC and the development of a combined source/channel coding scheme for SBC of images. Under the assumption of a noiseless channel, in an effort to develop more efficient subband coding schemes, we have tried to combine SBC ideas with other well-known coding techniques. It is in this vein that we have considered two different entropy-coded subband image coding schemes. In both schemes, all subbands except the lowest frequency subband (LFS) are quantized by zero-memory quantizers. In the first scheme (System A), the LFS is quantized by a predictive quantizer (DPCM) while in second scheme (System B) it is encoded by a 2-D DCT encoder. The quantizer outputs in both systems are entropy coded by means of Huffman codes. The performance results obtained after optimizing the system parameters are very encouraging as they suggest important performance improvements over the nonadaptive scheme in [2], and therefore, over all other schemes against which comparisons were made in [2]. However, these systems can be very sensitive to transmission noise. In fact, we will demonstrate that without some corrective measures, the two schemes developed here will be unacceptably sensitive to channel noise effects (much more than the scheme in [2]). To circumvent this problem, we have developed a combined source/channel coding scheme in which rate-compatible punctured convolutional codes are used for channel error protection. These systems perform dramatically better than their counterparts designed based on a noiseless channel. In all cases considered, the average performance of the channel-optimized systems is better than the performance of

the scheme in [2] over a noiseless channel.

The rest of this paper is organized as follows. Section II includes a brief discussion about the QMF bank. In Section III, the statistical properties of subbands are studied. The results of Section III provide the motivation for two SBC schemes described in Section IV. In this section, the two coding schemes are described and simulation results, including comparisons with the scheme in [2], are presented. Section V includes a study of the sensitivity of the systems in Section IV over a noisy channel. In Section VI, a combined source/channel coding scheme is described and simulation results over a variety of conditions are presented. Finally, Section VII contains a summary and conclusions.

II. Basic Structure of Subband Image Coders

In this section, we will briefly describe the structure of subband image coding systems; the reader is referred to [2] and [3] for details. The basic idea behind SBC is that of analyzing the original fullband image into a number of narrow-band images that are encoded and transmitted separately; the decoded subbands will then be used to synthesize a replica of the original image.

The analysis and synthesis are accomplished by using a QMF bank designed to eliminate the aliasing effects of bandpass filtering. Furthermore, 2-D QMF's can be separated into a cascade of two 1-D QMF's in each direction, which makes the actual implementation of the filters quite easy [2], [3]. The block diagrams of the 2-D separable QMF bank and the inverse QMF bank used for the analysis and synthesis of subbands are illustrated in Fig. 1. The analysis is performed by row filtering and 2-to-1 decimation followed by column filtering and 2-to-1 decimation. In Fig. 1, $H_1(z)$ indicates the transfer function of the 1-D QMF; for this filter we have used the 32-point 1-D QMF designated as 32D in [8]. The filtering was executed by spatial convolution in which the symmetric extension method proposed in [9] is used instead of the usual circular convolution to avoid the boundary effects. The superiority of this method is discussed in [9].

By applying the QMF bank, we can split the original fullband image into four equally-divided subbands referred to as the "*ll*", "*lh*", "*hl*" and "*hh*" subbands. Here, "*l*" and "*h*" are used to denote *low* and *high* frequencies, respectively. Each of these subbands is once more split into four equally-divided subbands by using the same QMF bank resulting in a total of 16 equally-divided subbands. The notation used to denote these 16 subbands is "$vw-xy$", where "vw" denotes the subband corresponding to the first stage and "xy" denotes the subband corresponding to the second stage. For example, '$ll-hl$" is used to denote the '*hl*" subband obtained from the second stage analysis of the "*ll*" subband of the first stage.

Each of the 16 subbands will be encoded by an appropriately designed encoder and transmitted to the receiver. The design of the encoder for different subbands is the major objective of this paper and will be discussed in the subsequent sections. In the receiver, the received signal is decoded and synthesized into the reconstructed image. For the synthesis, the decoded version of each of the 16 subbands is filtered, after 1-to-2 interpolation, by the same QMF in the column direction. The higher frequency subband is then subtracted from the lower frequency subband to generate a subband of double bandwidth. The same operation is repeated in the row direction to reconstruct four subbands. The same procedure is repeated on these four subbands to reconstruct a replica of the original image [2].

III. Statistical Properties of Subbands

In this section we summarize the results of our study of the statistical properties of the subbands. This includes the computation of the mean value, variance and correlation coefficients of each of the subbands. Also, in an effort to design "good" encoders, we study the shape of the distribution of subbands (for the LFS, we consider the distribution of the prediction residual or the 2-D DCT coefficients).

A. Mean Values, Variances and Correlations

To gain some insight about the statistical properties of the subband data, we have computed the mean, variance and correlation coefficients (row and column directions) of the different subbands for a variety of images. These results for a 512×512, 8-bit gray scale image called "LENA" (original image in Fig. 6.a) are summarized in Table I. It can be observed from these results that:

1. More than 95% of the total energy is contained in the LFS.
2. The mean value of all subbands except the LFS is very small compared with the standard deviation implying that in quantizing the subbands the mean value can be assumed to be zero.
3. The correlation properties of the LFS are similar to that of the original image. Therefore, conventional image coding techniques can be used to encode the LFS.
4. All subbands except the LFS have small correlation coefficients; this implies that little gain should be expected from exploiting the inter-pixel redundancies in these subbands.

Furthermore, we have investigated the cross-correlation between the subbands, and have found out that there is negligible cross-correlation between any pair of subbands. Based on these observations, we have decided to consider predictive quantization or 2-D DCT coding of the LFS and zero-memory quantization for other subbands.

B. Shape of the Distribution

Since the shape of the distribution plays an important role in the design of quantizers for different subbands, we have compared the empirical distribution of the subbands against that of the so-called *Generalized Gaussian Distribution* (GGD). The probability density function (pdf) associated with the GGD is given by [10]

$$p(x) = \left[\frac{\alpha\eta(\alpha,\beta)}{2\Gamma(1/\alpha)}\right] \exp\ \{-[\eta(\alpha,\beta)|x|]^{\alpha}\}\ , \tag{1a}$$

where

$$\eta(\alpha,\beta) = \beta^{-1}\left[\frac{\Gamma(3/\alpha)}{\Gamma(1/\alpha)}\right]^{\frac{1}{2}}\ , \tag{1b}$$

$\alpha > 0$ is a *shape parameter* describing the exponential rate of decay, β is the standard deviation of the distribution and $\Gamma(\cdot)$ is the gamma function. The GGD with $\alpha = 2.0$ coincides with the Gaussian pdf while for $\alpha = 1.0$ it becomes the Laplacian pdf. The GGD with α in the range $0.1 < \alpha < 1.0$ provides a useful model for broad-tailed densities [10].

Westerink *et al.* [11] reported that the distribution of subband data (except LFS) is approximated by the GGD with $\alpha = 0.5$ and that the prediction residual of the LFS is approximated by the GGD with $\alpha = 0.75$. It is not mentioned in [11], however, how these results are obtained. We have adopted the Kolmogorov-Smirnov (KS) test [12] as a distance

measure between the variance-normalized empirical distribution and the probability distribution function of the GGD with $\beta = 1.0$. The KS test was carried out for 12 different 8-bit monochrome images listed in Table II, which consist of 6 images of size 256×256 and 6 images of size 512×512. We have searched for the best value of α (in the sense of minimizing the KS distance) in the range $0.4 \leq \alpha \leq 2.0$. For each image, the best value of α for all subbands except the LFS as well as the best α for the prediction residual of the LFS is listed in Table III. Also, the best α obtained from the cumulative histograms (generated by accumulating the variance-normalized histograms of all images) is included in Table III. It can be concluded from these results that $\alpha = 0.7$ is a good approximation for the shape of the pdf of all subbands except the LFS; for the prediction residual of the LFS, $\alpha = 0.6$ is found to be best. Therefore, the pdf's under consideration are more broad-tailed than the Laplacian pdf which was assumed in [2] and [3]. In this sense, our results agree with those in [11], although there are some discrepancies in the specific values of α.

Since in our studies we will consider the 2-D DCT coding as a candidate for encoding the LFS, we have also conducted the KS test on the DCT coefficients of the LFS for blocksizes of 4×4, 8×8 and 16×16. We have considered the DC coefficient separately as its distribution appears to be considerably different from that of other coefficients. The results of the KS test for the DCT coefficients, summarized in Table IV, indicate that the best value of α is approximately 2.0 for the DC coefficient while it varies for other coefficients depending on the blocksize. For other coefficients, $\alpha = 0.6, 0.8$ and 1.0 were found to be best for blocksizes of 4×4, 8×8 and 16×16, respectively.

The values of α obtained in these tables will be used in the design of quantizers in the next section.

IV. Coding Schemes and Performance Results

In this section we describe the details of our two coding schemes and present simulation results obtained in encoding actual images.

A. Basic Approach

Our results in the previous section indicate that the LFS has statistical characteristics similar to those of the fullband image and hence conventional image coding techniques (predictive coding or transform coding) can be used for encoding it. All other subbands appear to have little intra-subband and inter-subband correlation and therefore zero-memory quantization should be adequate for encoding them. Based on these observations, we have confined attention to two encoding schemes described below.

1) *System A*: In this system the LFS is encoded by a predictive quantization scheme (DPCM) while the other subbands are quantized by zero-memory quantizers.

2) *System B*: In this system the LFS is encoded by a 2-D DCT coding scheme; the encoding of other subbands is similar to that of System A.

Recall from the results in Section III.B that the pdf of all subbands except the LFS is broad-tailed corresponding to the GGD with $\alpha = 0.7$; the same holds for the pdf of the prediction residual of the LFS with $\alpha = 0.6$. Similarly, the pdf of the 2-D DCT coefficients of the LFS are broad-tailed (the value of α depends on the DCT blocksize) with the exception of the DC coefficient which is almost Gaussian. In [10] the performance of zero-memory quantization schemes were studied for the class of GGD's. It was concluded that for broad-tailed distributions ($\alpha \leq 1.0$) (i) significant performance gains (in a rate-distortion theoretic

sense) can be obtained if optimum entropy-constrained quantizers (OECQ's) are used instead of Lloyd-Max quantizers (LMQ) and (ii) the rate-distortion performance of OECQ's is closely approximated by that of uniform-threshold quantizers (UTQ's). The added advantage of the UTQ over the OECQ is the simplicity of design and implementation. [1]

In view of the fact that the distributions of the subband data are quite broad-tailed and the conclusions in [10], it is reasonable to expect performance gains if the LMQ's of [2] are replaced by appropriately designed UTQ's. In both systems proposed above, UTQ will be used directly in quantizing all subbands except the LFS. In System A, a UTQ will be used to encode the prediction residual of the LFS, while in System B, UTQ's will be used to encode the 2-D DCT coefficients. In order to achieve an average bit rate close to the output entropy, the output of the UTQ's are encoded using Huffman codes (HC's). Therefore, the main design issues are:

1. the design of (UTQ,HC) pairs [2] to obtain performance close to the optimum performance theoretically attainable for the given value of α;
2. the optimal distribution of bits among the subbands. [3]

In the following we will elaborate on the design of (UTQ,HC) pairs and the bit allocation algorithm.

A.1. Entropy-Coded Quantization of Memoryless Sources

Consider a memoryless source distributed according to the GGD with a given parameter α. As indicated before, the performance of an N-level UTQ on this source can be easily obtained; if the number of quantization levels is sufficiently large, the performance will be very close to that of the OECQ [10]. An example of the performance of UTQ's with different number of levels (N=3,5,9,17,33,65,129) for the GGD with $\alpha = 0.6$ is illustrated in Fig. 2 (solid curves). For each N, the rate-distortion performance curve is obtained by varying the stepsize of the UTQ. Notice that the number of levels required for the UTQ to achieve performance close to the lower envelope depends on the encoding rate. For example, for the encoding rate of 1.5 bits/sample, $N = 5$ gives a performance far from the best performance (the lower envelope of all curves), whereas $N = 9$ gives a performance reasonably close to this lower envelope. Larger values of N do not result in a significant improvement, though they add to the complexity. Here, the encoding rate is the output entropy of the UTQ. However, in a practical situation, the output of the UTQ should be encoded by means of a noiseless source coding scheme to achieve an average encoding rate close to its entropy. In this paper, we consider the Huffman coding scheme. The performance of the UTQ's combined with HC's is also included in Fig. 2 (dotted curves). The order of the HC's used for N=3,5,9 and 17 is 5, 3, 2 and 2, respectively; for $N \geq 33$ 1st-order HC's were used. The selected choices of the order of the HC is a compromise between the performance of HC and its encoding complexity. It is evident from the curves in Fig. 2 that the average bit rates of the HC's are very close to the UTQ output entropy.

---

[1] An N-level UTQ is a symmetric quantizer with equi-spaced quantization thresholds in which the reconstruction levels are the centroids of the respective quantization intervals.

[2] The design of the UTQ involves the determination of the number of levels N and the stepsize Δ, while the design of the HC involves the determination of the order of the code as well as the actual coding table.

[3] Note that now the encoding rates used for different subbands are not limited to integer values (in contrast with the LMQ). This, in turn, introduces an additional degree of freedom which can result in performance improvements.

At this point, we need to select a set of (UTQ,HC) pairs to get a good approximation to the lower envelope of the rate-distortion performance of the UTQ's. To do this, for a fixed average bit rate, say r, we choose a combination of UTQ and HC that results in a small MSE without using a large N. In this way, we will obtain a compromise between performance and complexity. This is repeated for all values of r that are integer multiples of 0.1 bits/sample. The performance of this finite set of (UTQ,HC) pairs for the GGD with $\alpha = 0.6$ is illustrated in Fig. 3. In this figure, the lower envelope of the performance curves of all UTQ's is also included for comparison purposes. It can be seen from these results that this selected set of (UTQ,HC) pairs has a rate-distortion performance very close to the best performance.

The (UTQ,HC) pairs depicted in Fig. 3 are all obtained for $\alpha = 0.6$. This process is repeated for $\alpha = 0.7$, 0.8, 1.0 and 2.0. From now on, we will use the notation $d(r;\alpha)$ to denote the variance-normalized MSE associated with the (UTQ,HC) pair selected for operation at r bits/sample when the source is GGD with parameter α. Notice that this function is defined only for integer multiples of 0.1.

The next step in designing the system is the appropriate allocation of bits among the subbands. For system A, the bit allocation includes the predictive quantizer for the LFS and the zero-memory quantizers of other subbands. For System B, the bit allocation is over the zero-memory quantizers for the 2-D DCT of the LFS and the zero-memory quantizers of other subbands. In what follows we will elaborate on the bit allocation algorithm.

A.2 Bit Allocation

The overall MSE incurred in a subband coding scheme with K subbands is given by

$$D = \sum_{i=1}^{K} D_i(r_i), \tag{2a}$$

in which $D_i(r_i)$ is used to denote the distortion-rate performance of the encoder operating on the ith subband at r_i bits/sample. The encoding rate is given by [4]

$$R = \frac{1}{K}\sum_{i=1}^{K} r_i, \quad \text{bits/pixel.} \tag{2b}$$

In [2] a bank of *predictive coding* schemes was used to encode the subbands. The bit allocation algorithm used in [2] is based on the Lagrange multiplier techniques in which it was assumed that the distortion-rate performance of the predictive encoders are given approximately by $D_i(r_i) = 4.5 \cdot \sigma_{p,i}^2 \cdot 2^{-2r_i}$. Here, $\sigma_{p,i}^2$ is used to denote the variance of the prediction residual associated with the ith subband. Based on this assumption, the following bit allocation was obtained

$$r_i = r_{ave} + \frac{1}{2}\log_2 \left[\sigma_{p,i}^2 \Big/ \left(\prod_{i=1}^{K} \sigma_{p,i}^2 \right)^{\frac{1}{K}} \right], \; i = 1, 2, \cdots, K, \tag{3}$$

[4] In this paper we have assumed that all subbands have the same number of pixels. If this is not the case, the r_i's should be multiplied by appropriate weighting coefficients to account for the variability in the number of pixels per subband.

where r_{ave} is the design average bit rate. This result, however, is sub-optimal because it assumes an approximate relationship between the MSE and the bit rate of each of the predictive quantizers. Furthermore, this methods suffers from rate truncation problem as the r_i's must be *nonnegative* and *integer*.

In what follows we will describe an alternate approach for bit allocation in which the actual distortion-rate performances of the different quantizers are used for bit allocation. The algorithm is based on an integer programming algorithm described in a recent paper by Shoham and Gersho [13]. Since the distortion and rate are computed differently for Systems A and B, we will consider the two systems separately.

1) *System A*

In System A the LFS is encoded by a predictive quantizer while the other subbands are encoded by zero-memory quantizers. In view of our observations on the distribution of the prediction residual of the LFS and that of the other subbands, it is easy to show that the overall MSE can be written as

$$D_A = \sigma_{p,1}^2 d(r_1; 0.6) + \sum_{i=2}^{K} \sigma_i^2 d(r_i; 0.7), \tag{4a}$$

in which it is assumed that the LFS is the 1st subband and $\sigma_{p,1}^2$ denotes the variance of the prediction residual of the LFS. The encoding rate in this system is given by

$$R_A = \frac{1}{K} \sum_{i=1}^{K} r_i. \tag{4b}$$

2) *System B*

In System B the LFS is encoded by 2-D DCT; the encoding of the other subbands is the same as that in System A. Again based on observations on the distribution of the 2-D DCT coefficients (Section III.B), we can express the MSE by

$$D_B = \frac{1}{L^2} \{ \hat{\sigma}_{0,0}^2 d(r_{0,0}; 2.0) + \sum_{(j,k) \neq (0,0)} \hat{\sigma}_{j,k}^2 d(r_{j,k}; \alpha_L) \} + \sum_{i=2}^{K} \sigma_i^2 d(r_i; 0.7), \tag{5a}$$

where L is the blocksize of the 2-D DCT, α_L is the value of the shape parameter corresponding to blocksize L, $\hat{\sigma}_{j,k}^2$ is the variance of the (j,k)th transform coefficients and $r_{j,k}$ is the encoding rate associated with the (UTQ,HC) pair used for encoding the (j,k)th transform coefficient. The encoding rate in this case is given by

$$R_B = \frac{1}{K} \left\{ \frac{1}{L^2} \sum_{j=0}^{L-1} \sum_{k=0}^{L-1} r_{j,k} + \sum_{i=2}^{K} r_i \right\}. \tag{5b}$$

Recall that $\alpha_4 = 0.6$, $\alpha_8 = 0.8$ and $\alpha_{16} = 1.0$.

Now that the relationship between the overall distortion and encoding rate and the rate of individual UTQ's used in Systems A and B are determined, the bit allocation algorithm developed in [13] can be used straightforwardly to allocate bits (in multiples of

0.1) to the UTQ's used in the subband encoder. We will refer the reader to [13] for the details of the algorithm. For a prescribed *design* average rate, this algorithm results in a K-dimensional rate vector $(r_1^*, \cdots, r_K^*)$ for System A, and a $(L^2 + K - 1)$-dimensional rate vector $(r_{0,0}^*, \cdots, r_{L-1,L-1}^*, r_2^*, \cdots, r_K^*)$ for Systems B. Notice that the *actual* average bit rate may be slightly different from the design rate.

The rest of the coding scheme is straightforward. The LFS is encoded by means of a predictive quantization scheme or a 2-D DCT coding scheme; in both cases UTQ's followed by HC's are used to encode the data. The other subbands are encoded by UTQ's followed by appropriate HC's. In the receiver, the received codewords are decoded to obtain the quantized data. After reconstructing the LFS using the appropriate decoding scheme, a replica of the original image is reconstructed by using the 2-D separable inverse QMF bank on the decoded subbands. The block diagram of the two proposed systems is illustrated in Fig. 4.

B. Details of the Actual System Configuration

Having described the basic components of System A and System B, in what follows, we will present some additional details about the two systems.

1) *System A*

Since predictive quantization is used for the LFS in System A, we need to specify the predictor we have adopted. The predictor used is a linear predictor which predicts the value of the current pixel as a weighted summation of three neighboring pixels. Specifically, the predicted value of the pixel $X_{i,j}$ (ith row and jth column), say $\hat{X}_{i,j}$, is $\hat{X}_{i,j} = aX_{i,j-1} + bX_{i-1,j} + cX_{i-1,j-1}$, where a, b, and c are the predictor coefficients. We have optimized the value of a, b, and c for each image so as to minimize the mean squared prediction error. This can be done by solving the so-called Yule-Walker equations [14]. If we use the linearly separable auto-correlation functions, the optimal values of a, b, and c are $a = \rho_r, b = \rho_c$, and $c = -\rho_r\rho_c$, where ρ_r and ρ_c are the correlation coefficients in the row and column directions, respectively. Note that we have assumed that either the values of the correlation coefficients or the values of optimal predictor coefficients have to be transmitted to the receiver as side information.

We have to use two sets of (UTQ,HC) pairs in this system, one for the prediction residual of the LFS and the other for the higher frequency subbands. For both sets the allowed range of the average bit rate is from 0.0 to 5.0 bits/pixel in multiples of 0.1 bit/pixel. The exceptions are 0.1 and 0.2 bits/pixel because to achieve these bit rates we need HC's of order higher than five which makes the complexity of the HC prohibitive.

2) *System B*

In this system, the 2-D DCT is applied to the LFS. The $(L \times L)$ 2-D DCT and 2-D inverse DCT (IDCT) are described by [14]

$$\theta(j,k) = \frac{2}{L}\alpha(j)\alpha(k)\sum_{m=0}^{L-1}\sum_{n=0}^{L-1} x(m,n)\cos\frac{\pi j(2m+1)}{2L}\cos\frac{\pi k(2n+1)}{2L},$$

$$x(m,n) = \frac{2}{L}\sum_{j=0}^{L-1}\sum_{k=0}^{L-1} \alpha(j)\alpha(k)\theta(j,k)\cos\frac{\pi j(2m+1)}{2L}\cos\frac{\pi k(2n+1)}{2L},$$

where $\theta(j,k)$ represents the 2-D DCT of $x(m,n)$, and $\alpha(0) = 1/\sqrt{2}$, $\alpha(j) = 1$ for $j \neq 0$. The DC coefficients of the DCT are encoded by a (UTQ,HC) pair designed for the GGD

with $\alpha = 2.0$, while the higher order coefficients are quantized by (UTQ,HC) pairs optimally designed for the GGD with $\alpha = \alpha_L$. In addition, the mean values of the DC coefficients are transmitted separately. The allowed range of the average bit rate for the DC coefficients is from 2.0 to 8.0 bits/pixel, in multiples of 0.1. For other data including the higher order DCT coefficients and the higher frequency subbands, the allowed range is as in System A.

C. Simulation Results

Coding simulations were carried out for an 8-bit, 512×512 monochrome image (referred to as "LENA") selected from the images in Table I. This image is illustrated in Fig. 6.a. All simulations are based on $K = 16$ as in [2]. We have simulated Systems A and B described in this paper. Also, for comparison purposes we have simulated the system described by Woods and O'Neil in [2], hereafter referred to as the W-O scheme. In most cases, simulation results for design bit rates of 0.25, 0.5, 1.0, and 2.0 bits per pixel (bpp) are obtained.

The performance results in terms of peak signal-to-noise ratio (PSNR) for System A, System B with blocksize 4×4 and the W-O scheme are summarized in Table V and Fig. 5. It is evident from these results that the PSNR performance of System A and System B are almost identical; at very low bit rates System B offers a slight PSNR improvement over System A. Both System A and System B result in a significant improvement over the W-O scheme. This improvement in PSNR is approximately 3.5 dB at 0.25 bpp and larger than 4.5 dB at all other bit rates. [5]

For comparison purposes the reconstructed "LENA" for the three different schemes are presented in Figs. 6-8 for design bit rates of 0.25, 0.5 and 1.0 bpp. These results indicate that the subjective performance improvements offered by Systems A and B are quite significant. An interesting observation is the relative subjective performance of System B as compared to System A at 0.25 bpp. In this case, despite the very small PSNR improvement, the subjective improvement is quite noticeable and, in fact, the reconstructed image obtained from System B is clearly less "blotchy" in the flat (low activity) regions as compared to the image obtained from System A. In search of a reason for this clear discrepancy between objective and subjective performance results, we computed the average bit rates that was allocated to the LFS in System A and System B. Surprisingly, even this allocated bit rate to the LFS was the same and equal to 2.5 bpp. Thus, the only explanation for this superior subjective performance of System B, can be the inherent superiority of DCT coding over predictive quantization of images. We should add here that this subjective difference in performance was less noticeable at higher bit rates. A plausible explanation is that at higher bit rates the performance of DCT coding and predictive quantization become closer. Also, we should note that the "blockiness" effect inherent in DCT coding systems is not present here. This is because the allocated number of bits for LFS is quite large (at least 2.5 bpp).

We have also studied the effect of changing the 2-D DCT blocksize in System B. The results for different bit rates and blocksizes of 4×4, 8×8 and 16×16 are summarized in Table VI. It is clear from these results that no significant performance improvement can be obtained by increasing the blocksize. Indeed, in a few cases the increased blocksize results in a performance degradation. The reason for this rather surprising behavior, we feel, resides in

[5] Note that the actual average bit rates are somewhat different from the design rates specified in the bit allocation procedure. In fact, in all cases considered in Table V the actual bit rates of Systems A and B are below that of the W-O system. Taking this difference into account, the PSNR performance improvements at equalized bit rates are as high as 5.5 dB.

the following two observations. First, we should note that in our implementation of System B there is an explicit limitation on the largest number of bits allocated to the DCT coefficients (8.0 bpp for the DC coefficient and 5.0 bpp for others). We have observed that for blocksizes of 8×8 and 16×16, often times the assigned number of bits is equal to the upper limit indicating that perhaps these coefficients need to receive a larger number of bits - implying that the bit allocation is sub-optimal. The second observation is that the inter-pixel correlation in the LFS is smaller than that of the original image (due to the decimation process); consequently, the advantage of increased blocksize should be less pronounced. In view of these results, for the rest of the paper we will limit ourselves to a 4×4 blocksize for System B.

Before we close this subsection, we should mention that the performance of two other subband encoding schemes, namely those described in [3] and [6], are also included in Fig. 5. The performance results which are taken from [3] and [6] are also for the 512×512 "LENA" image and hence the comparisons are meaningful. It is evident from these results that Systems A and B perform better than both schemes. The comparisons with the results in [5] is not as simple because the image used in [5] is the 256×256 version of "LENA" for which a PSNR of approximately 27.9 dB at 0.5 bpp is reported (see Fig. 7 in [5]). However, we have simulated the performance of our systems on the 256×256 "LENA". The PSNR values are 30.94 dB at 0.48 bpp for both Systems A and B - approximately, 3 dB improvement.

D. Side Information

We conclude this section by evaluating the amount of side information which is to be transmitted to the receiver side.

Apart from the encoded data, the subband variances need to be transmitted as side (overhead) information. In addition, for System A the predictor coefficients need to be transmitted while in System B the variances of the DCT coefficients and the mean of the DC coefficient need to be transmitted. Note that if the variance information is available in the receiver, the bit allocation procedure can be repeated there and hence no additional information for the parameters of the (UTQ,HC) pairs is necessary.

Assuming that we need two bytes (16 bits) for each real-valued parameter, 36 bytes (16 subbands and 2 correlation coefficients) need to be transmitted for System A. This corresponds to 0.004 bpp for a 256×256 image and 0.001 bpp for a 512×512 image. In System B, in addition to the variances of the subbands, the variances of the DCT coefficients and the mean of the DC coefficient need to be transmitted. Therefore, for an $L \times L$ blocksize, the side information is $2(L^2 + 16)$ bytes. For the chosen blocksize of 4×4, this amounts to 0.008 bpp and 0.002 bpp for 256×256 and 512×512 images, respectively. Therefore, for all cases of interest the amount of side information is less than 0.01 bpp - a negligible amount.

V. Transmission Error Effects

In Systems A and B, variable-length coding is used extensively. It is well-known that, due to the sequential nature of decoding of such codes, channel errors could results in loss of synchronization, and hence, severe degradation in system performance. Furthermore, predictive coding (used in System A and the W-O scheme) is known to suffer from channel error propagation problems. Finally, in 2-D DCT coding (used in System B), channel errors propagate throughout the block. These facts indicate that the subband coding schemes studied in Section IV may suffer from serious difficulties in the presence of transmission (or storage) noise. Of course, due to the extensive use of variable-length coding in Systems A and

B, one would expect a greater sensitivity to channel noise in Systems A and B as compared to the W-O scheme. [6] In this section we will present simulation results for the performance of Systems A and B as well as the W-O scheme in the presence of channel noise.

To prevent the infinite propagation of decoding errors, we have packetized the codeword sequences before transmission. In what follows, we describe the details of the packetization scheme.

A. Packetization Scheme

The main motivation in packetization of codewords is to confine the propagation of channel noise to within a packet. To do so, we must make certain that our packets contain information about a fixed (or known in the receiver) number of pixels so that packet-to-packet error propagation is prevented. Since the pixels are encoded by variable-length codes, the packets cannot be of fixed length. However, in devising our packetization scheme we will try to keep the *average* packet length fixed so that fair comparisons can be made between different systems. It is important to remember that the severity of error propagation is directly related to the packet length.

In the packetization scheme adopted in this work, the packets consist of two parts: (i) a *length-indicator* indicating the length of the information portion (in bits) and (ii) the *information portion* consisting of a sequence of binary codewords. While the length of the length-indicator is fixed, that of the information portion of the packet could vary - hence resulting in *variable-length packets.* Furthermore, all codewords transmitted in a packet belong to the same subband. [7] To be more precise, let us consider a packet used for encoding the ith subband. Let us suppose that the pixels in this subband are encoded by means of HC's of order n_i at a design bit rate of r_i. Suppose the average length of the information portion of the packet is l_p bits. Then, the number of codewords in this packet is given by

$$n_{w,i} = \lceil \frac{l_p}{r_i n_i} \rceil \ , \tag{6}$$

where $\lceil x \rceil$ is used to denote the smallest integer greater than or equal to x. Because l_p is fixed and r_i and n_i are known from the results of the bit allocation procedure, $n_{w,i}$ can be determined in the receiver side. Therefore, in encoding the ith subband, each packet contains the information for $n_{p,i} = n_i n_{w,i}$ pixels. [8]

As for the decoding process, the following rules are applied:

1. Decoding of codewords in a packet starts and ends in that packet so that the decoding errors do not propagate beyond the packet boundaries.
2. Decoding of codewords in a packet associated with the ith subband terminates when one of the following three conditions is met:
   a. $n_{w,i}$ codewords are decoded,

[6] The W-O scheme also uses variable-length codes for encoding some subbands (see [2]); however, the LFS is encoded by fixed-length codes. Since the LFS has the highest variance among all subbands, the channel noise effects in the LFS should result in the most dramatic degradations in system performance.

[7] In System B, each of the transform coefficients is treated as a subband. Hence each packet contains codewords from only one transform coefficient.

[8] All packets used for encoding the ith subband contain $n_{p,i}$ pixels except possibly the last one which contains only the remaining pixels.

b. the decoding process reaches the end of a packet (known from the length-indicator),
c. a bit-string which cannot be decoded is encountered; in this case, decoding is stopped immediately, and all pixels that cannot be decoded are reconstructed as zero.

In what follows, we will present simulation results for the performance of the three schemes considered in Section IV when the channel is noisy.

B. Simulation Results over Noisy Channels

We assume that the channel is a memoryless binary symmetric channel (BSC) with a bit error rate (BER) of P_e. For our simulations in this section we have considered $P_e = 10^{-2}$, 10^{-3}, 10^{-4}, and 10^{-5}. To make certain that our results are meaningful, for each encoding scheme, bit rate and channel BER, we have repeated our simulations 50 times and computed the average PSNR (AVE-PSNR), maximum PSNR (MAX-PSNR), minimum PSNR (MIN-PSNR) and the standard deviation of the PSNR (STD-PSNR). Simulations are carried out for "LENA" encoded by Systems A and B and the W-O scheme [9] at design bit rates of 0.25, 0.5 and 1.0 bpp. The simulation results are summarized in Table VII. A few important observations about these results are in order.

1. System A is extremely sensitive to channel errors. Also, the STD-PSNR of System A is fairly large (especially for low BER's) implying that even at low channel BER's, there is a possibility of severe performance degradation (e.g., $\approx$ 14 dB difference between AVE-PSNR and MIN-PSNR for System A at 1.0 bpp with $P_e = 10^{-5}$).
2. System B is also very sensitive to channel errors. However, it performs considerably better than System A. In all cases considered the MIN-PSNR of System B was significantly larger (4-8 dB) than that of System A; the AVE-PSNR of System B was also larger than that of System A, especially for large values of the channel BER. Finally, the STD-PSNR of System B is smaller than that of system A.
3. The W-O scheme exhibits the highest degree of robustness in the presence of channel noise. In most cases, the effect of channel noise is negligible for $P_e < 10^{-3}$. Also, contrary to our observation for Systems A and B, the STD-PSNR in this case is very small. In almost all cases, the W-O system performs better than System B with the exception of a few cases where the channel noise is very small ($P_e = 10^{-5}$).

In Fig. 9, an example of reconstructed images from the three systems is presented for an encoding rate of 0.5 bpp and $P_e = 10^{-3}$; these images correspond to those cases in our simulation which result in the minimum PSNR. Clearly, the subjective performance of the three systems closely follow the trend suggested by the PSNR results of Table VII.

The results of Table VII (also supported by Fig. 9) suggest that Systems A and B, despite their superior performance for noiseless channels, exhibit an unacceptable level of sensitivity to channel errors and hence should not be used over noisy channels (at least over the range of channel BER's considered here). In the next section, we will describe a combined source/channel coding methodology to reduce this severe sensitivity to channel noise.

VI. Combined Source/Channel Coding

Systems A and B exhibit a high degree of sensitivity to channel noise because they have been designed to minimize the source coding distortion assuming a noiseless channel. It is a well-known fact that, in general, the more efficient the source coding scheme is, the more

[9] In all our simulations for noisy channels the average packet length is 1024 bits.

sensitive it will be to channel noise unless some corrective measures are taken. Specifically, it is shown in [15] for zero-memory quantizers and in [16] and [17] for predictive coding and transform coding of images, that in the presence of channel noise, increasing the accuracy of source encoder could result in an overall performance degradation.

One possible method for mitigating the channel error effects is use of error control coding. In this manner, of all bits used for encoding the image, some will be used in source coding while the rest will be kept to provide protection against channel noise. In [16] and [17], an approach in which specific source encoders and channel encoders are combined is considered; in this approach the rates of the source code and channel code are adjusted so as to minimize the MSE. In [15], an approach for channel-optimized quantization is developed in which source coding accuracy is traded for reduced sensitivity to channel noise.

In this paper, we will consider an approach similar to that of [16] and [17]. In our subband coding systems, an important question is how to distribute the bits among the source coding and channel coding operations for the different subbands so as to minimize the overall distortion caused by quantization noise and channel noise. The main difficulty in doing this stems from the fact that variable-length codes are used in Systems A and B. In this case, the analysis of channel error effects and its impact on the overall distortion is a formidable task (if not impossible).

Another important problem in our systems is that of bit allocation among the different subbands. Clearly, the bit allocation used under the noiseless channel assumption need not be optimal for noisy channels. To be able to determine the optimal bit allocation, we need to be able to determine the distortion-rate performance of the UTQ's followed by a HC and an error correcting code (ECC). Again, due to the inherent problems of packetized variable-length codes, the analytical computation of these distortion-rate performance results is not possible.

In what follows, we will describe a *simulation-based* procedure to determine the best (UTQ,HC,ECC) triple for encoding a memoryless source over a BSC at a given encoding rate. This procedure will lead to the determination of the distortion-rate performance functions that we need for optimal bit allocation among subbands.

A. Selection of (UTQ,HC,ECC) Triple and Bit Allocation

For the discussion in this subsection we will assume that the source is memoryless with a distribution corresponding to the GGD with parameter α and that the channel is a BSC with a BER given by P_e. Let us suppose for the time being that the ECC is to be selected from a prescribed family of ECC's. We will specify this family in the next subsection and provide justification for this choice.

For the given source and channel, consider a (UTQ,HC) pair (as selected in Section IV) with an average bit rate of r_s followed by an ECC with rate r_c and let $\hat{d}(r_s, r_c; \alpha, P_e)$ denote the MSE incurred in encoding and transmission of the source. Since the analytical computation of $\hat{d}$ is impossible, we have resorted to simulation [10] to determine its value for selected choices of r_s, r_c, α and P_e. Notice that the overall encoding rate is given by $r = r_s/r_c$.

Now consider a fixed encoding rate r. Among the available pairs of (r_s, r_c), there may be several that result in the encoding rate r. Let us denote by (r_s^*, r_c^*) the pair that minimizes

[10] As before, to obtain the MSE we have averaged our simulation results over 50 runs.

$\hat{d}(r_s, r_c; \alpha, P_e)$; denote this minimum distortion by $d_c(r; \alpha, P_e)$. In other words,

$$d_c(r; \alpha, P_e) = \min_{(r_s, r_c) \,:\, r_s/r_c = r} \hat{d}(r_s, r_c; \alpha, P_e). \tag{7}$$

The function $d_c(r; \alpha, P_e)$ determines the distortion-rate performance of the encoding scheme used for a source with parameter α and a BSC with BER P_e, after the appropriate selection of the (UTQ,HC,ECC) triple is made. Notice that for a fixed encoding rate r, identifying the pair (r_s^*, r_c^*) is equivalent to determining the optimal balance between the source coding accuracy and the channel error protection.

Having determined the $\hat{d}(r_s, r_c; \alpha, P_e)$ functions by simulation, we have computed the functions $d_c(r; \alpha, P_e)$ for values of α as in Section IV, $P_e = 10^{-2}, 10^{-3}$ and 10^{-4} and a finite number of values of r. [11] An example of the function $d_c(r; \alpha, P_e)$ is provided in Fig. 10 for $\alpha = 0.6$ and three different values of P_e. In this figure, different symbols are used to determine the rate of the optimum channel code used. Also, for comparison purposes, the distortion-rate performance of the (UTQ,HC) pairs of Section IV obtained for a noiseless channel is also included in this figure (dotted curve). The deviation between these performance curves and the one for the noiseless channel is merely the result of the channel noise. Obviously, the deviation is wider for more noisy channels.

Once the channel-optimized distortion-rate performances are determined the bit allocation procedure of Section IV can be used in a similar manner to obtain the optimum bit allocation among the subbands.

Before we present the simulation results for this combined source/channel coding scheme, in what follows we will describe the class of ECC's we have used in our systems.

B. Error Correction Coding Scheme

The ECC used in our system is a specific form of convolutional codes known as the *rate-compatible punctured convolutional* (RCPC) code. The RCPC code was introduced by Hagenauer [18] as an extension of the punctured convolutional code which was originally introduced by Cain *et al.* [19] mainly for the purpose of obtaining simpler Viterbi decoding for rate K/N (K$\neq$ 1) codes. The main advantage of the RCPC codes is that its rate (and hence the error correction capability) can be easily changed by varying the number of punctured bits in the puncturing matrix; therefore, with the same hardware, a variety of channel coding rates can be obtained. This is a desirable characteristic in our system as we wish to vary the rate of the ECC for each subband so as to obtain the best balance between the source coding rate and the channel coding rate. We should mention that this idea was first used in subband coding of speech [20] for adapting the degree of error protection to the error sensitivity of different coder bit streams.

The RCPC code is defined by a *generator tap matrix* of a convolutional code with the

[11] The actual computation of the $d_c(r; \alpha, P_e)$ function is slightly different from the above. Because there is only a finite number of r_s's and r_c's available, we have actually considered the set of all possible points $[\hat{d}(r_s, r_c; \alpha, P_e), r_s/r_c]$ in the distortion-rate plane and selected those that lie on the lower boundary of this set of points.

constraint length L_c

$$\mathbf{g} = \begin{array}{c} \\ N_c \\ \\ \end{array} \begin{array}{c} \overset{\leftarrow \quad L_c \quad \rightarrow}{} \\ \uparrow \\ \downarrow \end{array} \begin{pmatrix} & & \\ & g_{ik} & \\ & & \end{pmatrix}, \tag{8a}$$

which generates the *mother code* of rate $1/N_c$, and also by *puncturing matrices* with the puncturing period P_c,

$$\mathbf{a}(\ell) = \begin{array}{c} \\ N_c \\ \\ \end{array} \begin{array}{c} \overset{\leftarrow \quad P_c \quad \rightarrow}{} \\ \uparrow \\ \downarrow \end{array} \begin{pmatrix} & & \\ & a_{ij}(\ell) & \\ & & \end{pmatrix}, \qquad \ell = 1, 2, \ldots, (N_c - 1)P_c \tag{8b}$$

which determine the patterns of punctured bits. The nominal rate of the RCPC codes is given by

$$R_c = P_c/(P_c + \ell), \qquad \ell = 1, 2, \ldots, \ (N_c - 1)P_c, \tag{9}$$

which covers the range between $1/N_c$ and $P_c/(P_c + 1)$. In all of our studies, we have used the RCPC code shown in Table 1 in [18] with $N_c = 4$, $L_c = 5$, and $P_c = 8$. The generator tap matrix $\mathbf{g}$ and the puncturing matrices $\mathbf{a}(\ell)$ for $\ell = 1, 2, \ldots, 8$ are shown in Figs. 11 and 12, respectively.

It should be noted that R_c in (9) is not strictly equal to r_c used in (7) as the rate of the convolutional code. This is because $L_c - 1$ dummy bits should be added to the end of the source encoder output to return the state of the trellis to the all-zero state. Consequently, r_c is given by

$$r_c = [l_p R_c - (L_c - 1)]/l_p. \tag{10}$$

It should also be noted that when the combined source/channel coding scheme is used, the number of Huffman codewords per packet will be different from that in (6); in this case, the number of codewords in the packet associated with the ith subband is given by

$$n_{w,i} = \lceil r_{c,i} l_p / (r_{s,i} \cdot n_i) \rceil, \tag{11}$$

where $r_{s,i}$ and $r_{c,i}$ are the source and channel coding rates selected for encoding the ith subband and n_i is the same as in (6).

C. Simulation Results

In this section we will present simulation results for the performance of Systems A and B modified by the combined source/channel coding approach. From now on, the channel-optimized versions of System A and System B (with blocksize 4×4) will be called System C and System D, respectively. We have studied the performance of Systems C and D at design bit rates of 0.25, 0.5 and 1.0 bpp for channel BER's of 10^{-2}, 10^{-3} and 10^{-4}. In all cases, the same packetization scheme with $l_p = 1024$ was used. All subsequent simulation results are based on the 512×512 "LENA" image.

To provide some insight as to how the encoding rate is divided between the source coding and channel coding operations, in Table VIII we have included the average bit rate used for channel coding for different overall encoding rates. Notice that the percentage of bit rate dedicated to error control coding is larger for noisier channels - as one should expect. Also, in this table we have included the PSNR results corresponding to the case that the system is designed for a noisy channel but applied to a noiseless channel. These results provide an upper bound on the system PSNR over noisy channels. The difference between these upper bounds and the PSNR's of Table V are due to the lower rate used for source coding in Table VIII.

The performance of Systems C and D in terms of AVE-PSNR, MIN-PSNR, MAX-PSNR and STD-PSNR are summarized in Table IX for different channel BER's and encoding rates. The following important observations can be made.

1. Both System C and System D provide dramatic improvements over Systems A and B. The improvement of System C over System A is in the range 7 - 27 dB in AVE-PSNR. The improvement of System D over System B varies between 3 and 21 dB in AVE-PSNR. Typically, these improvements are larger at higher encoding rates and for noisier channels.
2. In all cases for both System C and System D, the MAX-PSNR coincides with the upper bound on PSNR listed in Table VIII. This means that bit errors caused by the noisy channel are sometimes perfectly corrected by the RCPC codes.
3. Almost in all cases, System D performs better than System C. Furthermore, System D exhibits a higher degree of robustness against channel noise. Typically, the difference between MAX-PSNR and MIN-PSNR is smaller in System D than in System C; the same holds for STD-PSNR. Since in both systems the same type of channel code is used, this superiority of System D must be due to the inherent robustness of 2-D DCT against transmission noise (similar to our observations in Section V).
4. Systems C and D perform better than the W-O scheme in the presence of channel noise (see Table VII). What is perhaps most interesting is that the performance of Systems C and D over a noisy channel is even better than that of the W-O scheme in the absence of channel noise. This has been our justification for not considering a channel-optimized version of the W-O scheme.

In Figs. 13 and 14 we present reconstructed images corresponding to MIN-PSNR and MAX-PSNR obtained from Systems C and D for the design rate of 0.5 bpp at two different values of channel BER, namely, $P_e = 10^{-2}$ and 10^{-3}. It is important to mention that the average quality of the reconstructed images in our simulations are usually closer to the image corresponding to MAX-PSNR rather than MIN-PSNR. This is especially true in System D.

D. Channel Mismatch

In designing Systems C and D it is assumed that the channel BER is known. In many practical situations the exact value of the BER is not known or the BER varies with time. In such situations it is important to know the amount of performance loss caused by channel mismatch. Let us denote by $PSNR(P_{e,d}, P_{e,a})$, the AVE-PSNR caused by a system designed for a channel with BER $P_{e,d}$ and applied to a channel with BER $P_{e,a}$. The $PSNR(P_{e,d}, P_{e,a})$ results for different values of $P_{e,d}$ and $P_{e,a}$ for both System C and System D are presented in Table X. These results are for an encoding rate of 0.5 bpp. We have observed that the trend of performance loss is the same for other bit rates.

The following important conclusions can be made:

1. System D is much more robust with respect to channel mismatch than System C.
2. Practically in all cases, the AVE-PSNR of the mismatched case with $P_{e,a} < P_{e,d}$ coincides with the MAX-PSNR of the *matched* case (i.e., when the system is designed and applied to a channel with BER $P_{e,d}$). This implies that in such cases, all channel errors are corrected by the RCPC codes used in the system.
3. To design the system, overestimating the channel BER is better than underestimating it. For example in System D, $|PSNR(10^{-2}, 10^{-3}) - PSNR(10^{-3}, 10^{-3})| = 1.17$ dB, while $|PSNR(10^{-3}, 10^{-2}) - PSNR(10^{-2}, 10^{-2})| = 6.59$ dB.

E. Side Information

As in Section IV, we need to evaluate the amount of side information necessary to be transmitted to the receiver for Systems C and D. In addition to the amount of side information evaluated in Section III, the following two items need to be transmitted:

1. the length-indicator of the packets, and
2. the additional bits for error protection of side information.

It is easy to show that the packet length can never be larger than 2^{14} bits; hence, 14 bits are enough to encode the length-indicator. [12] As for additional bits for protection of side information, we assume that a rate 1/3 RCPC code is powerful enough to render the side information error-free when the channel error probability is less than 10^{-2}. Under this assumption, the amount of side information of Section IV grows by a factor of three amounting to 0.013, and 0.023 bpp for Systems C and System D, respectively, for an image of size 256×256; for an image of size 512×512, the side information reduces by a factor of four. The length-indicator of a packet should also be protected because this information is indispensable for channel decoding. Assuming that 14 bits is used for the length-indicator, after error protection, 42 bits or six bytes are needed for the length-indicator. This increases the bit rate by $100 \times (6 \times 8/1024) = 4.7$ % corresponding to an increase of 0.012, 0.023, and 0.047 bpp for design average bit rates of 0.25, 0.5, and 1.0 bpp, respectively. In Table XI, we have summarized the increases of the average bit rate incurred by the side information. These numbers have to be added to the total bit rates tabulated in Table VIII to calculate the actual overall bit rates.

VII. Summary and Conclusions

In this paper, we have developed new schemes for subband image coding over noiseless and noisy channels. For the noiseless channel situation, we have developed two encoding schemes. The difference between the two schemes is in coding of the lowest frequency subband: the first scheme uses DPCM while the second uses 2-D DCT coding. Both schemes use zero-memory quantization for other subbands. An important feature of these schemes is that the output of all quantizers are entropy coded. The justification for using entropy-coded quantization resides in the statistical results on the shape of the distribution of subbands which suggest a significant gain for entropy-coded quantization over conventional Lloyd-Max quantization followed by fixed-length coding. Both schemes perform better than the non-adaptive scheme in [2] (and hence other schemes against which comparisons were made in [2]). The difference is significant both subjectively and objectively. The objective performances

[12] In all our simulations, the length of the packet has been less than 2^{11} bits.

of the DCT- and DPCM-based schemes are more-or-less the same, although at low bit rates, the DCT-based scheme offers a subjectively noticeable improvement over the DPCM-based scheme.

For noisy channels, due to the extensive use of variable-length codes and the concomitant error propagation problems, our schemes exhibit an unacceptable level of sensitivity to channel noise. To combat this difficulty, we have developed a combined source/channel coding scheme in which the schemes designed for the noiseless channel are combined with appropriately designed rate-compatible punctured convolutional codes. Simulation results for a variety of encoding rates and channel bit error rates indicate that the channel-optimized schemes perform dramatically better than their counterparts designed for the noiseless channel. They also perform better than the scheme developed in [2].

Fig. 15 illustrates the performance of the W-O scheme as well as Systems A, B, C and D at the encoding rate of 0.5 bpp. Clearly, Systems A and B exhibit a great sensitivity to channel noise, despite their very good performance for noiseless channels. Systems C and D both perform better than W-O. In fact, their worst performance (at $P_e = 10^{-2}$) is still better than the best performance (at $P_e = 0.0$) of W-O. System D performs better than System C and exhibits a better robustness against channel noise. In view of these results, we conclude that the best scheme among those considered here is System D. The DCT blocksize used in System D is 4×4, for which the complexity of implementation is quite manageable.

Possible avenues for further research include: (i) the study of intra-band entropy-constrained VQ [21] for encoding the subbands, (ii) the development of an extension of System B in which an *adaptive* 2-D DCT coding, similar to that of [22], is used for encoding the LFS and (iii) the study of system performance for bursty and fading channels.

References

1. R.E. Crochiere, S.A. Webber, and J.L. Flanagan, "Digital coding of speech in subbands," *Bell. Syst. Tech. J.*, vol. 55, pp. 1069-1085, Oct. 1976.
2. J.W. Woods and S.D. O'Neil, "Subband coding of images," *IEEE Trans. Acoust., Speech, Signal Processing*, vol. ASSP-34, pp. 1278-1288, Oct. 1986.
3. H. Gharavi and A. Tabatabai, "Sub-band coding of monochrome and color images," *IEEE Trans. Circuits and Systems*, vol. 35, pp. 207-214, Feb. 1988.
4. P.H. Westerink, J. Biemond, and D.E. Boekee, "Sub-band coding of images using predictive vector quantization," *Proc. ICASSP*, pp. 1378-1381, April 1987.
5. P.H. Westerink, D.E. Boekee, J. Biemond, and J.W. Woods, "Subband coding of images using vector quantization," *IEEE Trans. Commun.*, vol. COM-36, pp. 713-719, June 1988.
6. R.J. Safranek, K. Mackey, N.S. Jayant, and T. Kim, "Image coding based on selective quantization of the reconstruction noise in the dominant sub-band," *Proc. ICASSP*, pp. 765-768, April 1988.
7. C. Kim, J. Bruder, M.J.T. Smith, and R.M. Mersereau, "Subband coding of color images using finite state vector quantization," *Proc. ICASSP*, pp. 753-756, April 1988.
8. J.D. Johnston, "A filter family designed for use in quadrature mirror filter banks," *Proc. ICASSP*, pp. 291-294, April 1980.
9. M.J.T. Smith and S.L. Eddins, "Subband coding of images with octave band tree structures," *Proc. ICASSP*, pp. 1382-1385, April 1987.

10. N. Farvardin and J.W. Modestino, "Optimum quantizer performance for a class of non-Gaussian memoryless sources," *IEEE Trans. Inform. Theory*, vol. IT-30, pp. 485-497, May 1984.
11. P.H. Westerink, J. Biemond, and D.E. Boekee, "Evaluation of image sub-band coding schemes," *Proc. EURASIP*, pp. 1149-1152, Sept. 1988.
12. R.C. Reininger and J.D. Gibson, "Distributions of the two-dimensional DCT coefficients for images," *IEEE Trans. Commun.*, vol. COM-31, pp. 835-839, June 1983.
13. Y. Shoham and A. Gersho, "Efficient bit allocation for arbitrary set of quantizers," *IEEE Trans. Acoust., Speech, Signal Processing*, vol. ASSP-36, pp. 1445-1453, Sept. 1988.
14. N.S. Jayant and P. Noll, *Digital Coding of Waveforms.* Englewood Cliffs, NJ: Prentice-Hall, 1984.
15. N. Farvardin and V. Vaishampayan, "Optimal quantizer design for noisy channels: an approach to combined source-channel coding," *IEEE Trans. Inform. Theory*, vol. IT-33, pp. 827-838, Nov. 1987.
16. J.W. Modestino and D.G. Daut, "Combined source-channel coding of images," *IEEE Trans. Commun.*, vol. COM-27, pp. 1644-1659, Nov. 1979.
17. J.W. Modestino, D.G. Daut, and A.L. Vickers, "Combined source-channel coding of images using the block cosine transform," *IEEE Trans. Commun.*, vol. COM-29, pp. 1261-1274, Sept. 1981.
18. J. Hagenauer, "Rate-compatible punctured convolutional codes (RCPC codes) and their applications," *IEEE Trans. Commun.*, vol. COM-36, pp. 389-400, April 1988.
19. J.B Cain, G.C. Clark, Jr., and J.M. Geist, "Punctured convolutional codes of rate $(n-1)/n$ and simplified maximum likelihood decoding," *IEEE Trans. Inform. Theory*, vol. IT-25, pp. 97-100, Jan. 1979.
20. R.V. Cox, J. Hagenauer, N. Seshadri and C.-E. Sundberg, "A sub-band coder designed for combined source and channel coding," *Proc. ICASSP*, pp. 235-238, April 1988.
21. P.A. Chou, T. Lookabaugh and R.M. Gray, "Entropy-constrained vector quantization," *IEEE Trans. Acoust., Speech, Signal Processing*, vol. 37, pp. 31-42, January 1989.
22. W.-H. Chen and C. H. Smith, "Adaptive coding of monochrome and color images," *IEEE Trans. Commun.*, vol. COM-25, pp. 1285-1292, Nov. 1977.

TABLE I
STATISTICS OF 16 SUBBANDS OF "LENA"

Image	Mean Value	Variance	Correlation Coefficient	
			Row	Column
Original	124.0	2290	0.969	0.984
LL-LL	124.1	2223	0.862	0.934
LL-LH	-0.010	10.86	-0.121	-0.488
LL-HL	-0.008	31.96	-0.401	0.201
LL-HH	0.015	8.101	-0.209	-0.379
LH-LL	-0.006	0.586	0.064	-0.028
LH-LH	0.009	1.325	-0.017	0.293
LH-HL	0.004	0.486	0.021	-0.095
LH-HH	0.024	1.536	-0.019	0.341
HL-LL	-0.019	1.610	-0.161	0.114
HL-LH	0.007	0.872	-0.125	-0.120
HL-HL	-0.020	5.405	0.280	0.150
HL-HH	-0.001	2.412	0.285	-0.196
HH-LL	0.003	0.371	-0.031	-0.049
HH-LH	0.004	0.521	-0.054	0.089
HH-HL	0.001	0.468	0.074	-0.082
HH-HH	-0.008	0.860	0.148	0.227

TABLE II

STATISTICS OF 12 IMAGES USED IN KOLMOGOROV-SMIRNOV TEST

Image Name	Size	Mean Value	Variance	Correlation Coefficient	
				Row	Column
GIRL	256 × 256	58.8	1579	0.970	0.958
COUPLE		33.4	1000	0.931	0.952
WOMAN		99.2	2734	0.934	0.968
MOON		127.2	824	0.907	0.906
HOUSE		138.1	2131	0.974	0.951
TREE		129.2	4551	0.967	0.925
LENA	512 × 512	124.0	2290	0.969	0.984
PEPPER		120.2	2903	0.973	0.976
BABOON		129.6	1790	0.865	0.752
SAILBOAT		125.2	4296	0.973	0.970
AIRPLANE		179.2	2154	0.960	0.961
TIFFANY		211.1	858	0.920	0.922

TABLE III

RESULTS OF KOLMOGOROV-SMIRNOV TEST FOR ALL SUBBANDS EXCEPT LFS AND PREDICTION RESIDUAL OF LFS

Image Name	Size	Best Value of α	
		All Subbands Except LFS	Prediction Residual of LFS
GIRL	256 × 256	0.65	0.55
COUPLE		0.60	0.50
WOMAN		0.60	0.60
MOON		1.15	0.80
HOUSE		0.70	0.55
TREE		0.75	0.80
Average for 256×256		0.70	0.60
LENA	512 × 512	0.75	0.45
PEPPER		0.80	0.50
BABOON		0.85	1.05
SAILBOAT		0.85	0.55
AIRPLANE		0.65	0.50
TIFFANY		0.60	0.55
Average for 512×512		0.75	0.55
Average for All		0.70	0.60

TABLE IV
RESULTS OF KOLMOGOROV-SMIRNOV TEST
FOR 2-D DCT COEFFICIENTS OF LFS

Test Data \ DCT Blocksize / Coeff.		4	8	16
6 Images of Size 256×256	DC	2.0	2.0	2.0
	Others	0.60	0.85	1.50
6 Images of Size 512×512	DC	2.0	2.0	2.0
	Others	0.60	0.75	0.90
All Images	DC	2.0	2.0	2.0
	Others	0.60	0.75	1.00

TABLE V
BIT RATE AND PSNR VALUES (IN dB) FOR
RECONSTRUCTED "LENA"

System \ Design Rate		0.25	0.5	1.0	2.0
System A	Actual Rate	0.24	0.45	0.89	1.94
	PSNR	32.00	35.16	38.55	43.82
System B (4×4)	Actual Rate	0.24	0.45	0.89	
	PSNR	32.19	35.32	38.53	
W-O	Actual Rate	0.25	0.51	1.04	2.19
	PSNR	28.65	29.94	34.01	38.61

TABLE VI
BIT RATE AND PSNR VALUES (IN dB) FOR
RECONSTRUCTED "LENA" FROM SYSTEM B

Block Size \ Design Rate		0.25	0.5
4×4	Actual Rate	0.24	0.45
	PSNR	32.19	35.32
8×8	Actual Rate	0.23	0.44
	PSNR	32.19	35.26
16×16	Actual Rate	0.24	0.45
	PSNR	32.07	35.11

TABLE VII

PSNR PERFORMANCE RESULTS (IN dB) FOR "LENA" AT DESIGN BIT RATE OF (a) 0.25 BPP, (b) 0.5 BPP, (c) 1.0 BPP

System \ Channel BER		1×10^{-2}	1×10^{-3}	1×10^{-4}	1×10^{-5}
System A	AVE-PSNR	9.86	14.24	23.21	30.64
	MAX-PSNR	10.69	16.23	31.99	32.00
	MIN-PSNR	9.17	11.82	16.48	20.58
	STD-PSNR	0.40	1.00	3.08	3.02
System B (4×4)	AVE-PSNR	14.33	21.12	28.40	31.54
	MAX-PSNR	15.40	24.07	31.93	32.19
	MIN-PSNR	13.42	18.52	23.55	24.53
	STD-PSNR	0.54	1.50	2.49	1.57
W-O	AVE-PSNR	22.93	27.62	28.54	28.64
	MAX-PSNR	24.09	28.03	28.65	28.65
	MIN-PSNR	21.86	27.10	28.36	28.54
	STD-PSNR	0.51	0.22	0.06	0.04

(a)

TABLE VII (CONTINUED)

System \ Channel BER		1×10^{-2}	1×10^{-3}	1×10^{-4}	1×10^{-5}
System A	AVE-PSNR	7.46	13.17	23.73	31.89
	MAX-PSNR	8.27	15.86	34.66	35.16
	MIN-PSNR	6.97	10.29	18.27	21.37
	STD-PSNR	0.32	1.16	3.41	4.31
System B (4×4)	AVE-PSNR	13.90	20.32	29.81	34.77
	MAX-PSNR	14.94	24.56	35.04	35.32
	MIN-PSNR	13.12	17.33	23.58	28.18
	STD-PSNR	0.45	1.62	2.97	1.44
W-O	AVE-PSNR	23.08	28.52	29.77	29.93
	MAX-PSNR	24.38	29.07	29.94	29.94
	MIN-PSNR	20.88	27.29	29.57	29.78
	STD-PSNR	0.60	0.32	0.08	0.04

(b)

TABLE VII (CONTINUED)

System \ Channel BER		1×10^{-2}	1×10^{-3}	1×10^{-4}	1×10^{-5}
System A	AVE-PSNR	7.43	12.83	23.92	34.59
	MAX-PSNR	8.64	16.72	36.57	38.55
	MIN-PSNR	6.65	9.77	17.81	20.29
	STD-PSNR	0.34	1.48	4.45	4.96
System B (4×4)	AVE-PSNR	14.03	20.65	31.01	37.49
	MAX-PSNR	15.32	23.82	35.74	38.53
	MIN-PSNR	13.03	18.59	23.23	27.88
	STD-PSNR	0.51	1.45	3.05	1.88
W-O	AVE-PSNR	21.92	29.81	33.33	33.94
	MAX-PSNR	23.71	31.08	33.94	34.01
	MIN-PSNR	20.16	28.14	32.11	33.12
	STD-PSNR	0.72	0.65	0.38	0.17

(c)

TABLE VIII

DISTRIBUTION OF BITS BETWEEN SOURCE CODING AND CHANNEL CODING FOR "LENA" AT DESIGN RATES OF (a) 0.25 BPP, (b) 0.5 BPP, (c) 1.0 BPP

System \ Channel BER		1×10^{-2}	1×10^{-3}	1×10^{-4}
System C	Total Bit Rate	0.26	0.25	0.25
	Channel Bit Rate (%)	0.11 (42%)	0.05 (20%)	0.05 (18%)
	PSNR	29.66	30.92	31.03
System D	Total Bit Rate	0.25	0.24	0.24
	Channel Bit Rate (%)	0.11 (45%)	0.06 (26%)	0.04 (15%)
	PSNR	30.10	31.02	31.65

(a)

System \ Channel BER		1×10^{-2}	1×10^{-3}	1×10^{-4}
System C	Total Bit Rate	0.49	0.46	0.46
	Channel Bit Rate (%)	0.22 (45%)	0.11 (24%)	0.08 (17%)
	PSNR	32.49	33.86	34.35
System D	Total Bit Rate	0.48	0.46	0.45
	Channel Bit Rate (%)	0.22 (45%)	0.11 (25%)	0.07 (15%)
	PSNR	32.73	34.10	34.56

(b)

System \ Channel BER		1×10^{-2}	1×10^{-3}	1×10^{-4}
System C	Total Bit Rate	0.91	0.88	0.87
	Channel Bit Rate (%)	0.42 (46%)	0.20 (23%)	0.14 (16%)
	PSNR	35.39	37.14	37.56
System D	Total Bit Rate	0.91	0.89	0.88
	Channel Bit Rate (%)	0.41 (45%)	0.22 (24%)	0.14 (16%)
	PSNR	35.60	37.05	37.59

(c)

TABLE IX

PSNR PERFORMANCE RESULTS (IN dB) FOR "LENA" IN THE PRESENCE OF CHANNEL NOISE AT DESIGN BIT RATE OF (a) 0.25 BPP, (b) 0.5 BPP, (c) 1.0 BPP

System \ Channel BER		1×10^{-2}	1×10^{-3}	1×10^{-4}
System C	AVE-PSNR	27.16	29.60	30.91
	MAX-PSNR	29.66	30.92	31.03
	MIN-PSNR	18.98	20.40	27.15
	STD-PSNR	3.28	2.40	0.56
System D	AVE-PSNR	29.96	30.94	31.49
	MAX-PSNR	30.10	31.02	31.65
	MIN-PSNR	28.62	29.46	30.52
	STD-PSNR	0.27	0.25	0.30

(a)

TABLE IX (CONTINUED)

System \ Channel BER		1×10^{-2}	1×10^{-3}	1×10^{-4}
System C	AVE-PSNR	30.74	32.91	34.30
	MAX-PSNR	32.49	33.86	34.35
	MIN-PSNR	21.60	26.59	33.97
	STD-PSNR	2.96	1.93	0.08
System D	AVE-PSNR	32.38	33.90	34.46
	MAX-PSNR	32.73	34.10	34.56
	MIN-PSNR	26.39	29.00	33.78
	STD-PSNR	0.92	0.72	0.17

(b)

TABLE IX (CONTINUED)

System \ Channel BER		1×10^{-2}	1×10^{-3}	1×10^{-4}
System C	AVE-PSNR	34.34	35.73	37.50
	MAX-PSNR	35.39	37.14	37.56
	MIN-PSNR	24.87	22.61	37.12
	STD-PSNR	2.52	3.15	0.11
System D	AVE-PSNR	35.24	36.71	37.53
	MAX-PSNR	35.60	37.05	37.59
	MIN-PSNR	32.10	32.88	37.12
	STD-PSNR	0.58	0.66	0.10

(c)

TABLE X

CHANNEL MISMATCH PERFORMANCE RESULTS AT 0.5 BPP; (a) SYSTEM C, (b) SYSTEM D

$P_{e,a}$ \ $P_{e,d}$		1×10^{-2}	1×10^{-3}	1×10^{-4}	0.0
1×10^{-2}	AVE-PSNR	30.74	18.71	9.32	7.46
	MAX-PSNR	32.49	22.65	11.42	8.27
	MIN-PSNR	21.60	16.31	7.66	6.97
	STD-PSNR	2.96	1.29	0.87	0.32
1×10^{-3}	AVE-PSNR	32.49	32.91	29.16	13.17
	MAX-PSNR	32.49	33.86	34.10	15.86
	MIN-PSNR	32.49	26.59	20.91	10.29
	STD-PSNR	0.0	1.93	4.76	1.16
1×10^{-4}	AVE-PSNR	32.49	33.86	34.30	23.73
	MAX-PSNR	32.49	33.86	34.35	34.66
	MIN-PSNR	32.49	33.86	33.97	18.27
	STD-PSNR	0.0	0.0	0.08	3.41
0.0	PSNR	32.49	33.86	34.35	35.16

(a)

TABLE X (CONTINUED)

$P_{e,a}$ \ $P_{e,d}$		1×10^{-2}	1×10^{-3}	1×10^{-4}	0.0
1×10^{-2}	AVE-PSNR	32.38	25.79	18.78	13.90
	MAX-PSNR	32.73	28.37	20.82	14.94
	MIN-PSNR	26.39	22.87	16.76	13.12
	STD-PSNR	0.92	1.33	1.17	0.45
1×10^{-3}	AVE-PSNR	32.73	33.90	32.54	20.32
	MAX-PSNR	32.73	34.10	34.49	24.56
	MIN-PSNR	32.73	29.00	23.47	17.33
	STD-PSNR	0.0	0.72	2.42	1.62
1×10^{-4}	AVE-PSNR	32.73	34.10	34.46	29.81
	MAX-PSNR	32.73	34.10	34.56	35.04
	MIN-PSNR	32.73	34.10	33.78	23.58
	STD-PSNR	0.0	0.0	0.17	2.97
0.0	PSNR	32.73	34.10	34.56	35.32

(b)

TABLE XI
THE AMOUNT OF SIDE INFORMATION (BPP)

Image Size \ Design Rate / System		0.25	0.5	1.0
256 × 256	System C	0.025	0.036	0.060
	System D	0.035	0.046	0.070
512 × 512	System C	0.015	0.026	0.050
	System D	0.018	0.029	0.053

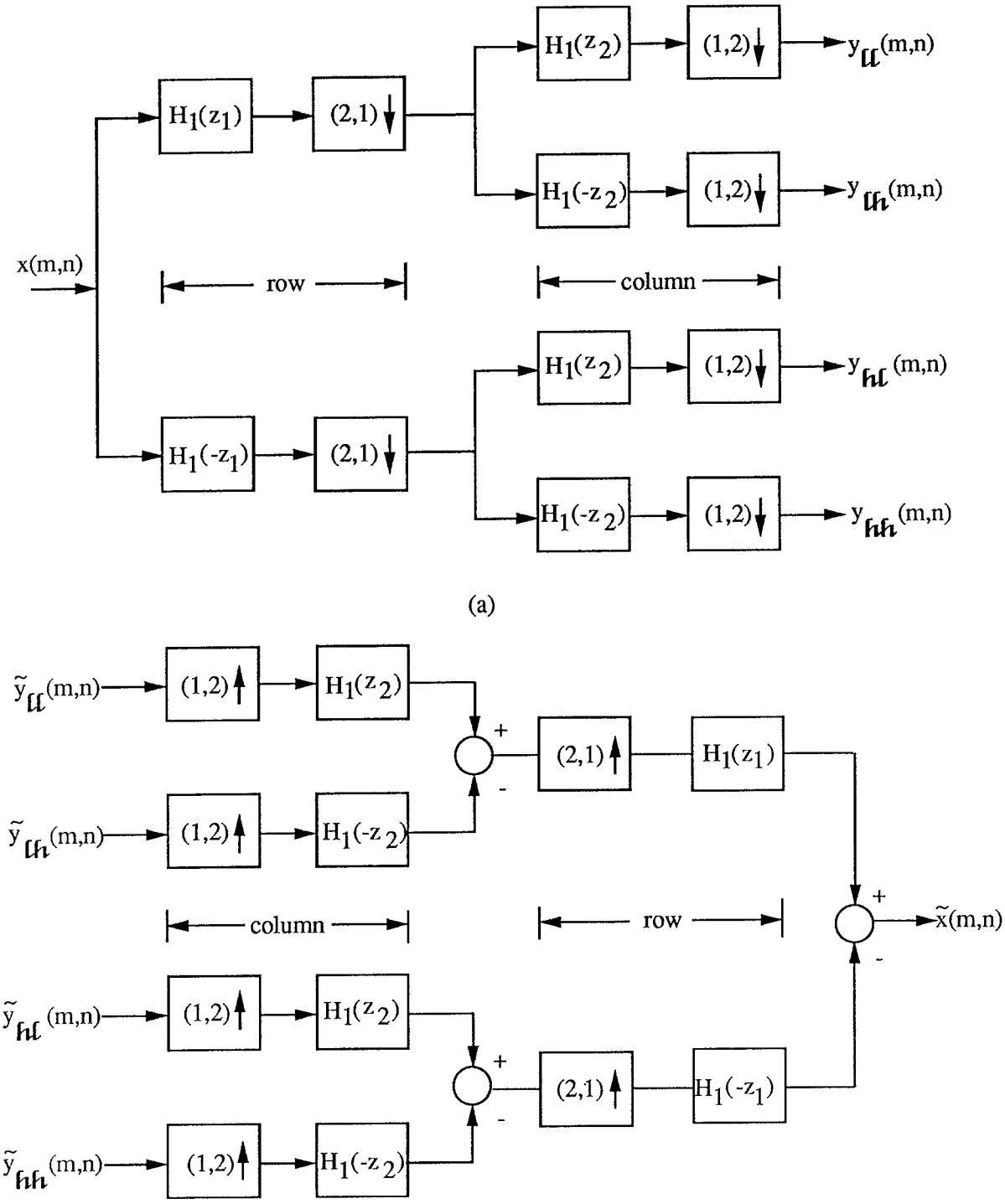

Figure 1:
(a) 2-D Separable QMF Bank, (b) 2-D Separable Inverse QMF Bank;
"↓" and "↑" Denote 2-to-1 Decimation and 1-to-2 Interpolation, Respectively.

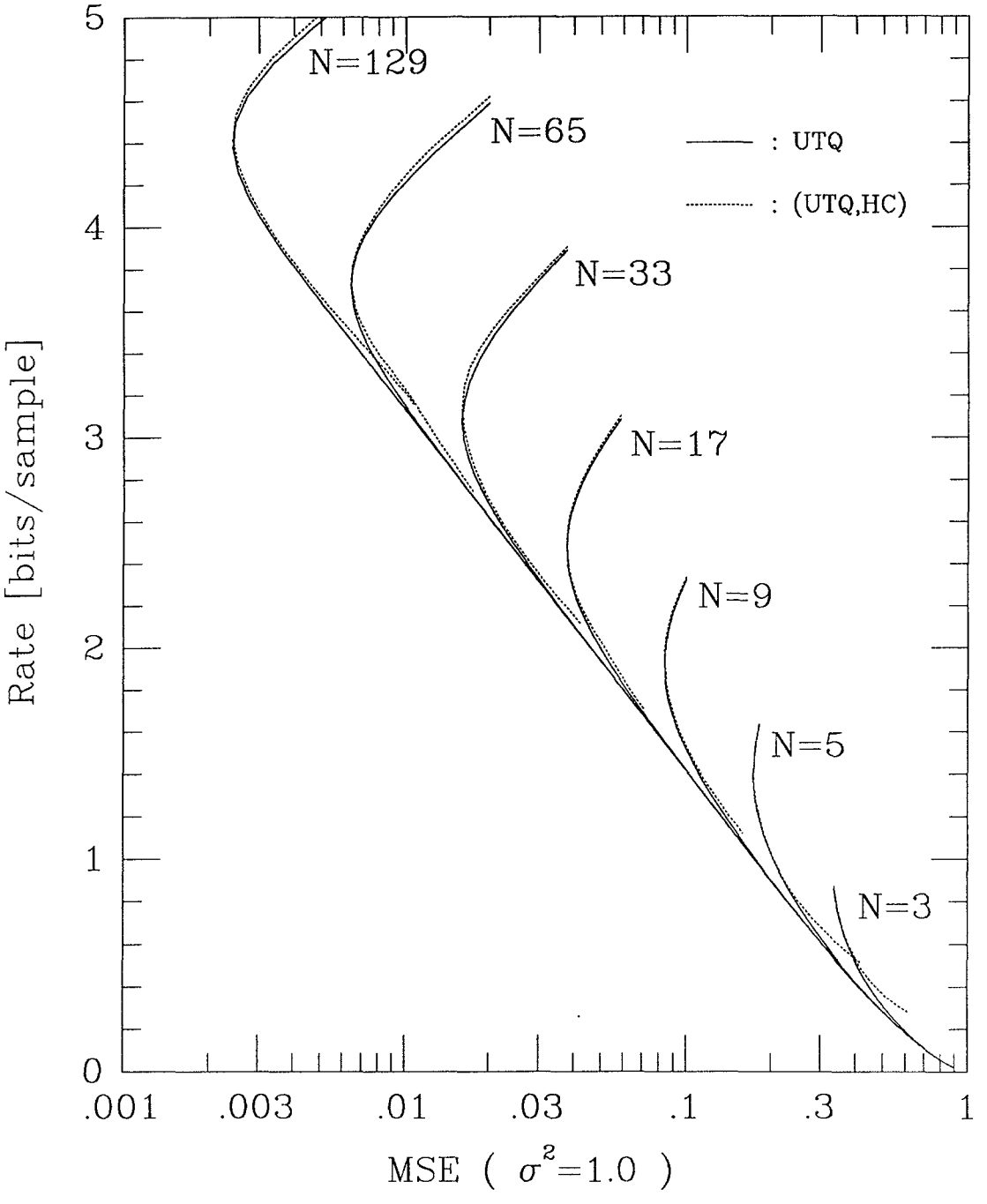

Figure 2: Rate-Distortion Performance of (UTQ, HC) Pairs for Different Number of Levels; α =0.6.

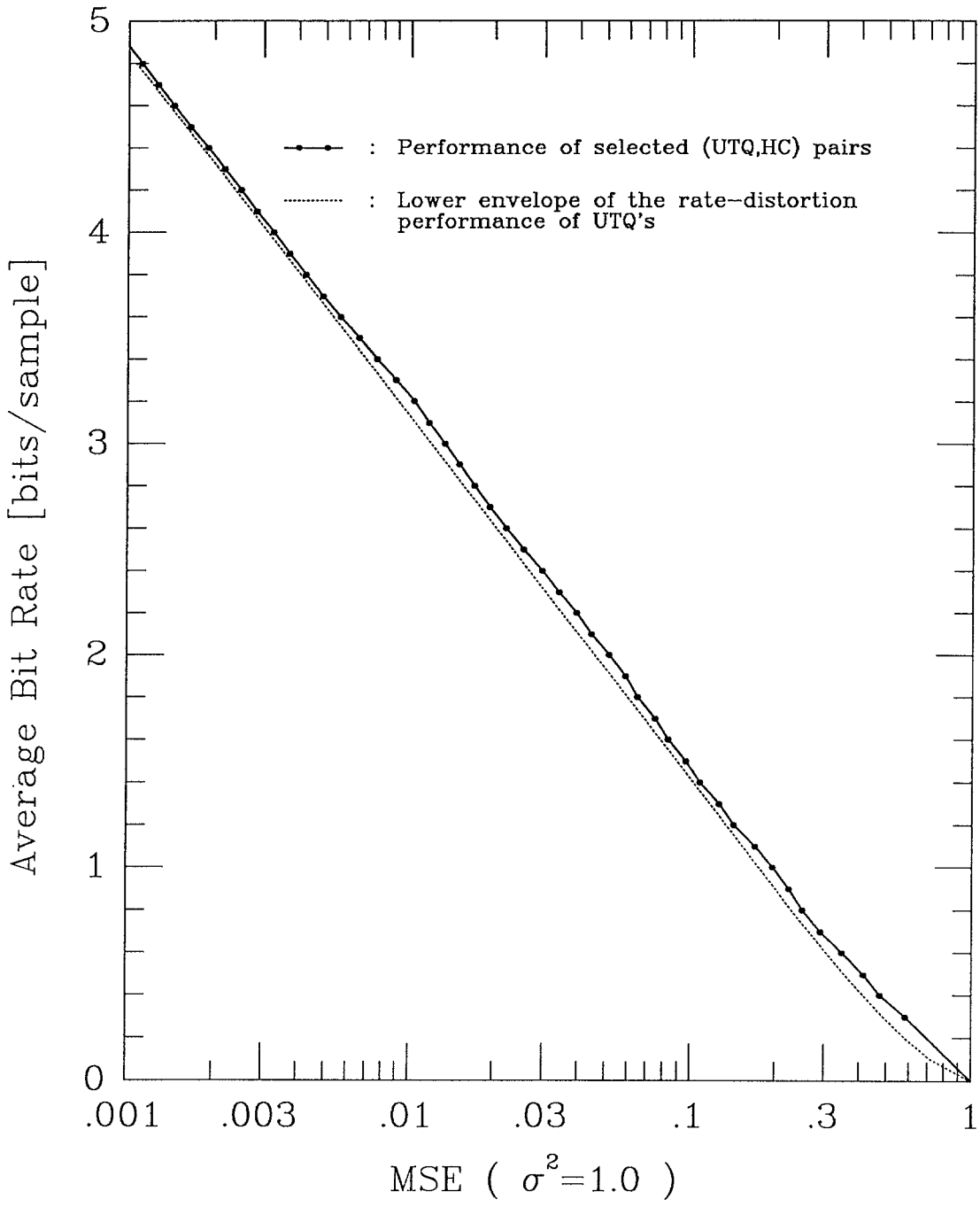

Figure 3: Rate-Distortion Performance of the Selected Set of (UTQ, HC) Pairs; α=0.6.

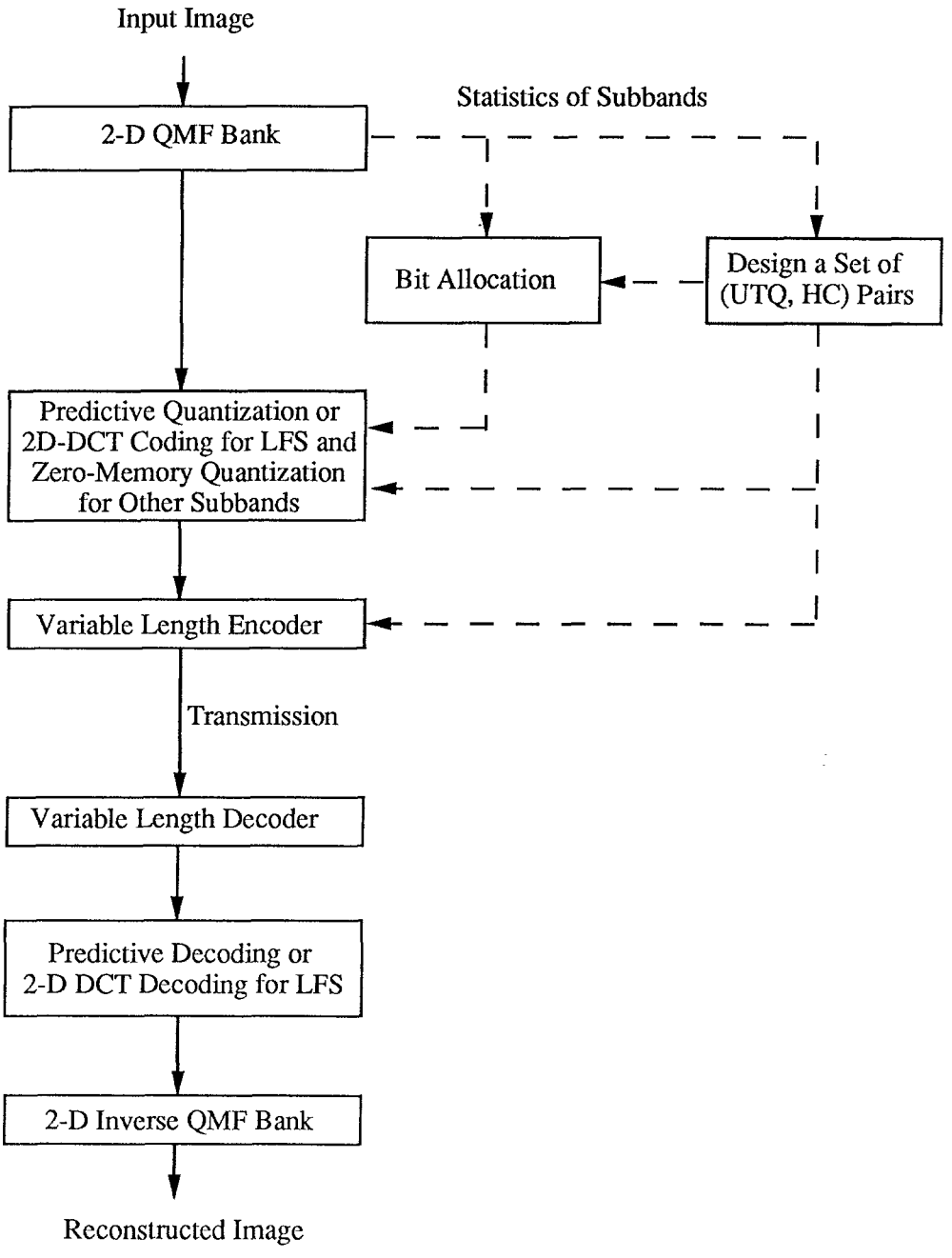

Figure 4: Block Diagram of Systems A and B.

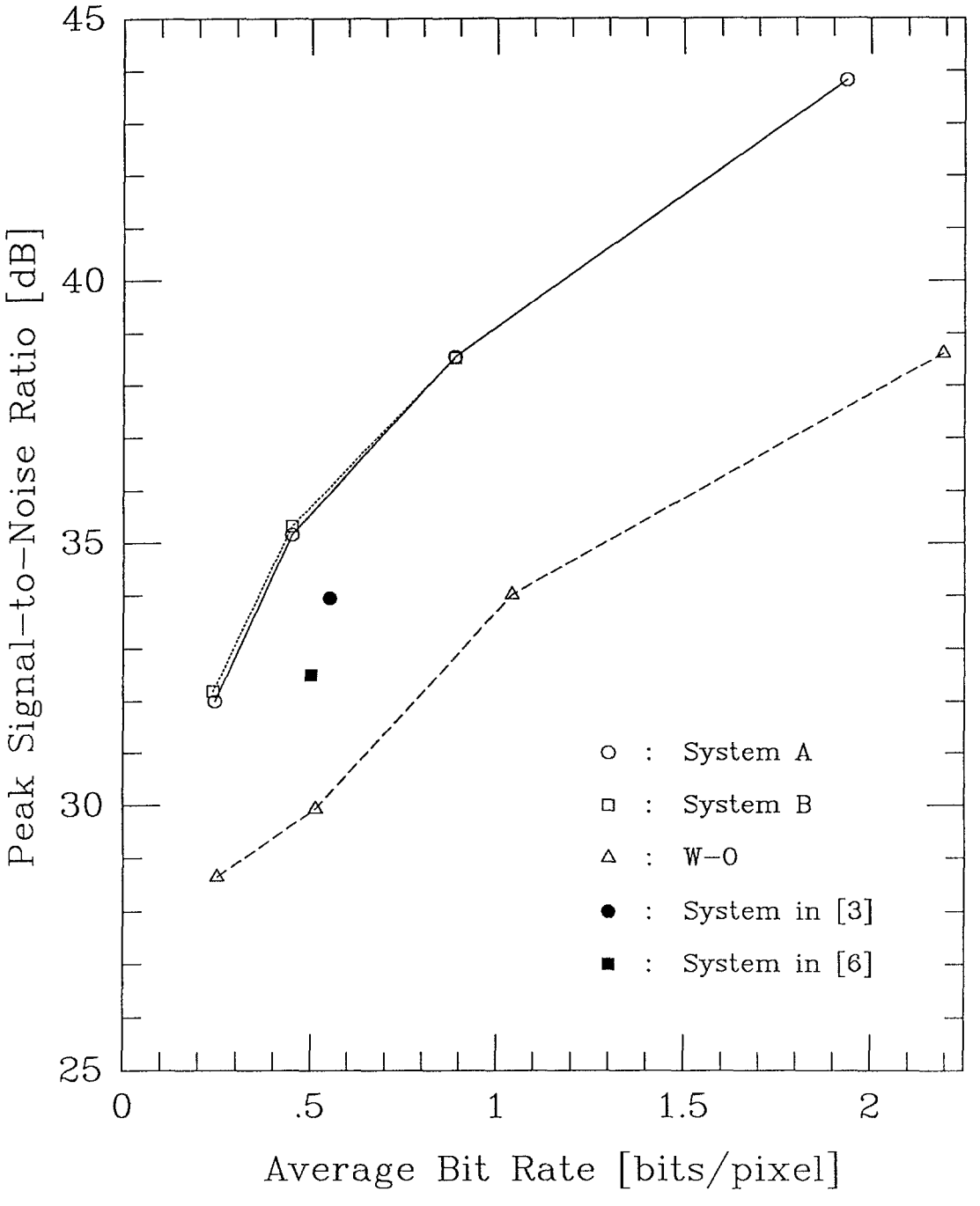

Figure 5: PSNR's of Reconstructed "LENA" for System A, System B and W-O.

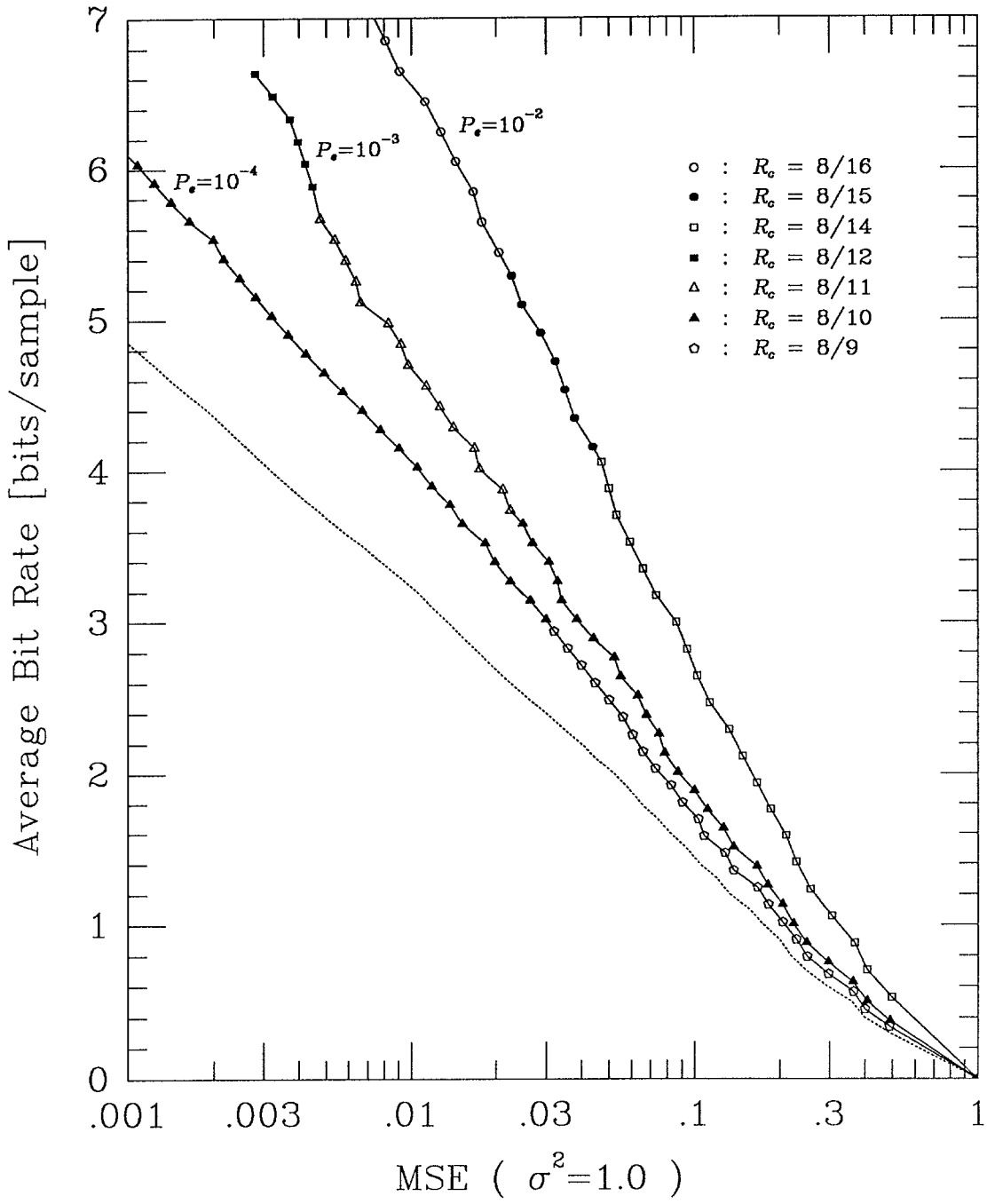

Figure 10: Rate-Distortion Performance of the Selected Set of (UTQ, HC, ECC) Triples; α=0.6.

$$g = \begin{bmatrix} 1\,0\,1\,1\,0 \\ 1\,1\,1\,0\,1 \\ 1\,0\,1\,1\,1 \\ 1\,1\,0\,1\,1 \end{bmatrix}$$

Figure 11: The Generator Tap Matrix.

$$a(1) = \begin{bmatrix} 1\,1\,1\,1\;0\,1\,1\,1 \\ 1\,0\,0\,0\;1\,0\,0\,0 \\ 0\,0\,0\,0\;0\,0\,0\,0 \\ 0\,0\,0\,0\;0\,0\,0\,0 \end{bmatrix} \qquad a(2) = \begin{bmatrix} 1\,1\,1\,1\;1\,1\,1\,1 \\ 1\,0\,0\,0\;1\,0\,0\,0 \\ 0\,0\,0\,0\;0\,0\,0\,0 \\ 0\,0\,0\,0\;0\,0\,0\,0 \end{bmatrix}$$

$$a(3) = \begin{bmatrix} 1\,1\,1\,1\;1\,1\,1\,1 \\ 1\,0\,1\,0\;1\,0\,0\,0 \\ 0\,0\,0\,0\;0\,0\,0\,0 \\ 0\,0\,0\,0\;0\,0\,0\,0 \end{bmatrix} \qquad a(4) = \begin{bmatrix} 1\,1\,1\,1\;1\,1\,1\,1 \\ 1\,0\,1\,0\;1\,0\,1\,0 \\ 0\,0\,0\,0\;0\,0\,0\,0 \\ 0\,0\,0\,0\;0\,0\,0\,0 \end{bmatrix}$$

$$a(5) = \begin{bmatrix} 1\,1\,1\,1\;1\,1\,1\,1 \\ 1\,1\,1\,0\;1\,0\,1\,0 \\ 0\,0\,0\,0\;0\,0\,0\,0 \\ 0\,0\,0\,0\;0\,0\,0\,0 \end{bmatrix} \qquad a(6) = \begin{bmatrix} 1\,1\,1\,1\;1\,1\,1\,1 \\ 1\,1\,1\,0\;1\,1\,1\,0 \\ 0\,0\,0\,0\;0\,0\,0\,0 \\ 0\,0\,0\,0\;0\,0\,0\,0 \end{bmatrix}$$

$$a(7) = \begin{bmatrix} 1\,1\,1\,1\;1\,1\,1\,1 \\ 1\,1\,1\,1\;1\,1\,1\,0 \\ 0\,0\,0\,0\;0\,0\,0\,0 \\ 0\,0\,0\,0\;0\,0\,0\,0 \end{bmatrix} \qquad a(8) = \begin{bmatrix} 1\,1\,1\,1\;1\,1\,1\,1 \\ 1\,1\,1\,1\;1\,1\,1\,1 \\ 0\,0\,0\,0\;0\,0\,0\,0 \\ 0\,0\,0\,0\;0\,0\,0\,0 \end{bmatrix}$$

Figure 12: The Puncturing Matrices.

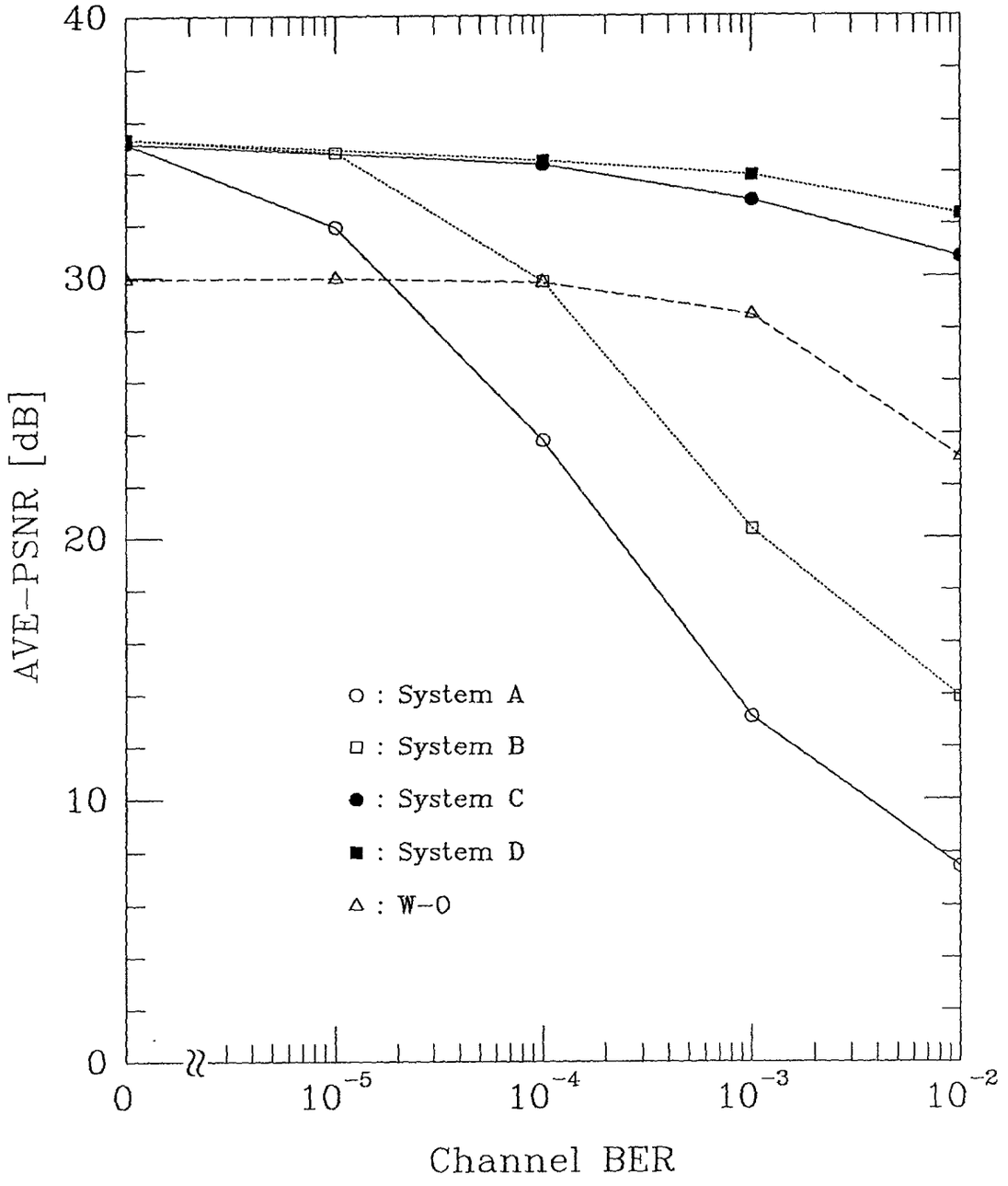

Figure 15: AVE-PSNR Performance of Systems A, B, C, D and W-O for Different Channel BER's at Design Rate of 0.5 bpp.